

Modular Subsurface Sensors and Integrated Software for Advanced Subsurface Characterization and Monitoring using Unoccupied Vehicles

August 2024

Matthew Taubman
Anton Sinkov
Esteban Bowles-Martinez
Luke Placzek
Lisa Newburn
Amoret Bunn
John Smart
Frederick Day-Lewis

DISCLAIMER

This report was prepared as an account of work sponsored by an agency of the United States Government. Neither the United States Government nor any agency thereof, nor Battelle Memorial Institute, nor any of their employees, makes **any warranty, express or implied, or assumes any legal liability or responsibility for the accuracy, completeness, or usefulness of any information, apparatus, product, or process disclosed, or represents that its use would not infringe privately owned rights.** Reference herein to any specific commercial product, process, or service by trade name, trademark, manufacturer, or otherwise does not necessarily constitute or imply its endorsement, recommendation, or favoring by the United States Government or any agency thereof, or Battelle Memorial Institute. The views and opinions of authors expressed herein do not necessarily state or reflect those of the United States Government or any agency thereof.

PACIFIC NORTHWEST NATIONAL LABORATORY
operated by
BATTELLE
for the
UNITED STATES DEPARTMENT OF ENERGY
under Contract DE-AC05-76RL01830

Printed in the United States of America

Available to DOE and DOE contractors from
the Office of Scientific and Technical Information,
P.O. Box 62, Oak Ridge, TN 37831-0062

www.osti.gov

ph: (865) 576-8401

fox: (865) 576-5728

email: reports@osti.gov

Available to the public from the National Technical Information Service
5301 Shawnee Rd., Alexandria, VA 22312

ph: (800) 553-NTIS (6847)

or (703) 605-6000

email: info@ntis.gov

Online ordering: <http://www.ntis.gov>

Modular Subsurface Sensors and Integrated Software for Advanced Subsurface Characterization and Monitoring using Unoccupied Vehicles

August 2024

Matthew Taubman
Anton Sinkov
Esteban Bowles-Martinez
Luke Placzek
Lisa Newburn
Amoret Bunn
John Smart
Frederick Day-Lewis

Prepared for
the U.S. Department of Energy
under Contract DE-AC05-76RL01830

Pacific Northwest National Laboratory
Richland, Washington 99354

Abstract

The advent and subsequent proliferation of autonomous airborne, waterborne, and ground-based vehicles (i.e., “drones”) promises to broadly transform the geosciences and associated industries, including fossil energy exploration and development, mineral resource exploration and development, water-resource management, and environmental remediation. For geophysical characterization and monitoring, the prospect of programming highly repeatable and low-cost drone missions for subsurface imaging will allow for deployments in hazardous and previously inaccessible areas. Coupled with autonomous workflows for data processing, management, and visualization, drone-based geophysical characterization and monitoring will enable unprecedented, real-time insight into diverse subsurface properties and processes of scientific and engineering importance. Toward this end, the objectives of this Lab Directed Research and Development (LDRD) project were to develop (1) new instrumentation for drone-based electromagnetic induction (EMI) geophysical imaging, including separated transmitter and receivers and associated electronics and (2) new software for real-time data telemetry, processing, management, and visualization. Although EMI has been previously deployed using unoccupied aerial systems (UASs), these applications failed to capitalize on the game-changing capabilities of drone platforms. Whereas drone-based data acquisition allows for collection of rich, three-dimensional (3D) multi-offset/multi-angle configurations between transmitters and receivers, past efforts have relied on conventional instrumentation that was designed for ground-based data collection with the transmitter and a single receiver housed in the same unit; nor did these previous applications demonstrate real-time delivery of results to support rapid management decisions in the field.

In this 1-year project, we (1) designed and constructed new lightweight independent transmitter and receiver antenna platforms that communicate with a laptop computer; (2) developed software to control data acquisition, manage/transfer data, and visualize data as its collected; and (3) demonstrated the operation of the new hardware and software systems in a ground-based field test. Our work entails major technological advances for EMI and established a foundation on which to build a new drone-based, real-time geophysical EMI imaging capability to support diverse challenges facing the nation.

Acknowledgments

This research was supported by the Energy Mission Seed Investment, under the Laboratory Directed Research and Development (LDRD) Program at Pacific Northwest National Laboratory (PNNL). PNNL is a multi-program national laboratory operated for the U.S. Department of Energy (DOE) by Battelle Memorial Institute under Contract No. DE-AC05-76RL01830.

Acronyms and Abbreviations

3D – Three-dimensional

Ω – Ohm / Ohms

μF – microfarads

ADC – Analog to digital converter

AWG – American wire gauge

Cap – Capacitor

CLK – Clock

COTS – Commercially available off-the-shelf

DC – Direct current

DDS – Direct digital synthesis, and/or digital synthesizer board

DOI – Depth of investigation

EC – Electrical conductivity

EMF – Electromotive force

EMI – Electromagnetic induction

GPS – Global positioning system

GUI – Graphical user interface

HDF5 – Hierarchical data format 5

IN AMP – Instrumentation amplifier

INSITE – PNNL Agile LDRD investment entitled Induced Spectral Imaging Technology for the Environment

kHz – Kilohertz

LDRD – Laboratory-directed research and development

MEMS – Micro Electronic Mechanical Systems

mH - millihenries

MHz – Megahertz

nF – nanofarads

OEM – Original Equipment Manufacturer

pF - picofarads

PNNL – Pacific Northwest National Laboratory

R&D – Research and development

Rx – Receiver

SOM – System on module

TCP – Transmission communication protocol

Tx – Transmitter

UAS – Unoccupied aerial systems

VSP – Visual Sample Plan

Contents

Abstract.....	ii
Acknowledgments.....	iii
Acronyms and Abbreviations.....	iv
1.0 Introduction	1
2.0 Background	4
3.0 Approach.....	6
4.0 Detail.....	7
4.1 Instrumentation Hardware.....	7
4.1.1 Receiver (Rover).....	8
4.1.2 Transmitter (Base)	12
4.1.3 Common Elements	16
4.2 Software	16
5.0 Field demonstration.....	20
6.0 Discussion & Conclusions	24
7.0 References.....	25

Figures

Figure 1. Tradeoffs between (a) time required for a geophysical survey and spatial data coverage, and (b) time required for a survey and spatial data coverage. (Mangel et al., 2022).....	1
Figure 2. (a) Photograph showing the standard operation of the Geophex GEM-2 instrument, which houses transmitter and receiver antennas in a ski-shaped tool, and (b) photograph showing the use of UAS with the GEM-2. (Photographs from https://geophex.com/).	2
Figure 3. Schematic of the operation of a horizontal coplanar frequency domain electromagnetic system.	5
Figure 4. Left shows a picture of the receiver platform (rover) taken before field testing. The platform is a 24- by 48-inch by 5/8-inch thick sheet of plywood, with subcomponents attached using plastic hardware. Moving from the top of the figure down to the bottom are seen the receiver coil (aka antenna), the receiver electronics board, and finally the batteries. Right shows a photo of all the subelements of the electronics board before assembly, including the radio, RS-422 digital adapter (422), INSITE analog to digital / microcontroller board, precision clock (CLK), digital synthesizer (DDS), and GPS.	9
Figure 5. Block diagram of receiver platform. This shows interconnections as well as DC power requirements.	10
Figure 6. Left shows the winding process of the receiver coil former using AWG18 enameled copper wire. Care had to be taken to pack the turns in	

carefully so that wires from adjacent layers didn't come close to one another. Right shows the finished receiver coil. The coil has an inductance of 2.67 millihenries, a DC resistance of 1.09Ω, and a self-resonance of 298.5 kHz. 11

Figure 7. Impedance analyzer response of finished receiver coil showing a self-resonance of 298.5 kHz. 11

Figure 8. Photograph of the Tx platform (base) taken before field testing. The platform is a 38- by 68-inch by 5/8-inch thick sheet of plywood, with subcomponents attached using plastic hardware. Moving from the top of the figure down to the bottom are seen the Tx coil (aka antenna), the resonating capacitor unit and power amplifier (gray boxes), current sensing meter, signal generation board (INSITE intermediate node board) and batteries. 12

Figure 9. Block diagram of transmitter platform. This shows interconnections as well as DC power requirements. 13

Figure 10. Photographs showing the process of winding the 24-inch Tx coil. Large plastic disks had to be used to support the open-frame coil during this process. 81.3 turns were wound out of an expected 100, of 18-AWG wire. 14

Figure 11. Impedance analyzer response of finished transmitter coil showing a self-resonance of 90.83 kHz. 15

Figure 12. Photo of the capacitor box used to resonate the Tx coil. This consists of three parallel banks of caps, each consisting of a series string of two. Two of these strings comprise 220-nF caps, while the smaller central one comprises 47-nF caps. This gives a total capacitance of 243.5 nF. 15

Figure 13. Screen capture of the GUI for measurement acquisition and control and real-time visualization of data in the field. 17

Figure 14. Screen capture of the digital object description for the HDF5 database in which the drone data are organized. 18

Figure 15. Analytical modeling result showing the transmitter coil, generated primary magnetic field, and receiver coil measuring this. 19

Figure 16. Photograph of field test setup, showing transmitter (larger black coil), roving receiver cart and coil, field laptop, and electronics. 20

Figure 17. Photograph of field test site, the "south field" at the southern end of the PNNL campus. 20

Figure 18. Raw EMI data collected in the field test, displayed. The Tx was located midway along the transect, where magnitude is greatest. The effect of two metallic targets is clearly visible. 21

Figure 19. Photograph of field test, with field laptop in the foreground, showing the GUI, Tx in the middle ground, and roving Rx cart in the background. 22

Figure 20. Observed EMI data collected in the field test (blue) and data corrected (orange) to remove the effect of the primary field (green) using the analytical model. 23

1.0 Introduction

Geophysical methods are used increasingly to support characterization and monitoring challenges across the applied geosciences, including fossil energy exploration and development, mineral resource exploration and extraction, water resource management, and environmental remediation. Over the last two decades, geophysical research and development (R&D) has steadily evolved toward more rapid acquisition, processing, and delivery of results in efforts to make geophysical information more actionable and supportive of end users' needs (e.g., Johnson et al., 2022). Perhaps the most active and transformative area of geophysical research today involves the application of new drone technologies in geophysical data acquisition, as evidenced by numerous special issues of journals, vision papers, and special journal sections devoted to the topic (e.g., Mangel et al., 2022). Deployed as airborne, waterborne, and ground-based platforms for data acquisition and/or sampling, drones provide cost-effective access to remote areas, reduce risk to human operators, and allow for highly repeatable surveys. It has been suggested that drone-based geophysical surveys will achieve spatial data coverage approaching that of airborne/satellite-based geophysics while also achieving the resolution of ground-based geophysics (Figure 1).

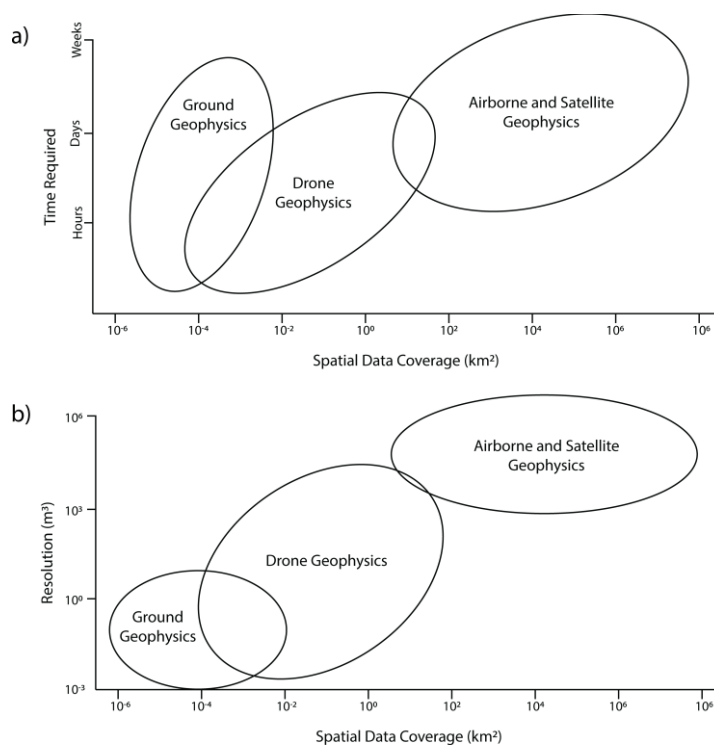


Figure 1. Tradeoffs between (a) time required for a geophysical survey and spatial data coverage, and (b) time required for a survey and spatial data coverage. (Mangel et al., 2022).

Common payloads for small unoccupied airborne systems (UAS) include thermal cameras (Harvey et al., 2019), multi- and hyperspectral cameras (Scholl et al., 2024), and, increasingly, geophysical instrumentation (e.g., Mangel, 2022). Among geophysical methods, frequency-domain EMI is particularly suited to integration with drone technology. By adjusting

transmitter/receiver offsets, and transmitter/receiver orientations, the resolution and depth of investigation can be optimized for project-specific needs; furthermore, EMI provides information about diverse subsurface targets. EMI primarily senses variations in electrical conductivity (EC), which is related to soil or rock type, the presence of metallic infrastructure, voids, moisture content, porosity, salinity (total dissolved solids), and, in some cases, the presence of contamination. EMI is well-suited to time-lapse operation for change detection (e.g., Terry et al., 2023). Compared to electrical and seismic techniques, EMI requires no electrodes, geophones or other instrumentation coupled to the ground; thus, it can be performed entirely from the air.

EMI geophysical surveys are offered commercially (e.g., <https://www.dronegeosci.com/>), but significant R&D is required to fully capitalize on the potential of drone technology for EMI. Currently, contractors rely on conventional EMI instrumentation, such as the Geophex GEM-2¹, which was developed for ground-based surveys (Figure 2). In the GEM-2 and similar instruments, the transmitter (Tx) and receiver (Rx) antennas (coils) are housed in the same unit or otherwise connected by cables to a common controller; consequently, it is not possible to capitalize on the potential of drones for flying multiple receivers simultaneously or acquiring data at a variety of Tx/Rx offsets and orientations.

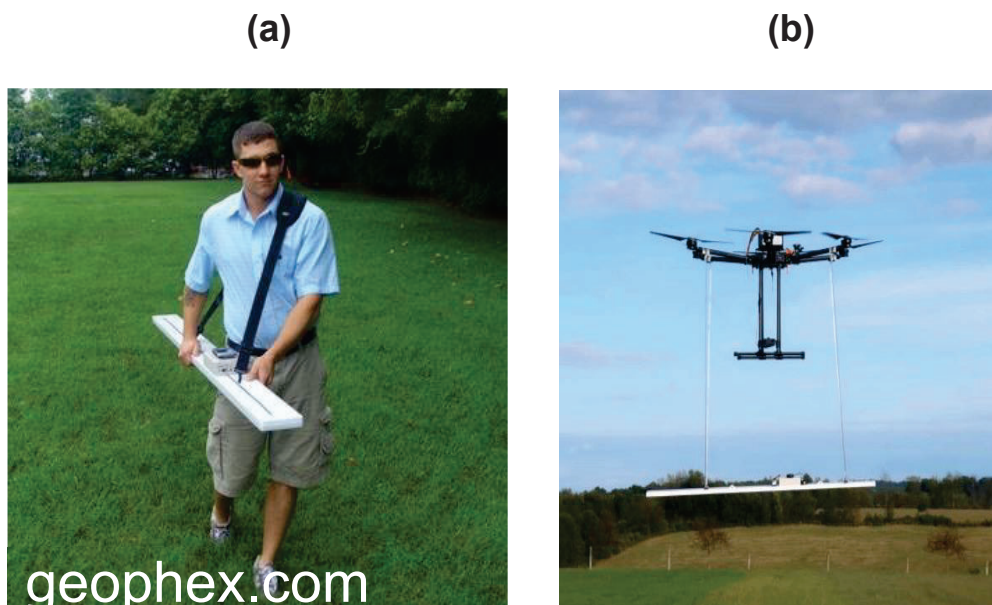


Figure 2. (a) Photograph showing the standard operation of the Geophex GEM-2 instrument, which houses transmitter and receiver antennas in a ski-shaped tool, and (b) photograph showing the use of UAS with the GEM-2. (Photographs from <https://geophex.com/>).

Under this 1-year Lab Directed Research and Development (LDRD) project, we sought to advance EMI instrumentation and data processing to capitalize more fully on the potential of drone technology. This work was motivated by four technical objectives:

¹ Use of trade names is for informational purposes only and does not imply endorsement.

- (1) To design and construct new lightweight Tx and Rx antennas that are housed independently (i.e., not physically connected), thus enabling use of multiple receivers and variable Tx/Rx offsets and configurations
- (2) To develop geophysical payloads that satisfy forward looking security requirements for 'blue technology';
- (3) To develop software to control data acquisition, manage/transfer data, and visualize data in near real-time, as the data are collected; and
- (4) To demonstrate the operation of the new hardware and software systems in a ground-based field test.

This project leveraged the Pacific Northwest National Laboratory's (PNNL's) experience and expertise in instrument design, real-time geophysical data analysis, and geophysical field demonstrations.

2.0 Background

The frequency-domain EMI method is commonly used for mapping and (or) imaging near-surface (a few tens of meters) EC variations (Ward and Hohmann, 1988), and the closely related controlled-source electromagnetic method (CSEM) is used for imaging deeper (10's to 100's of meters) (Jaysaval et al., 2014; Zhdanov, 2009). Typical EMI instruments house two coplanar wire loop antennas within a single tool, such as the GEM-2 (Figure 2). An oscillating current is driven at a specified frequency through one antenna coil (i.e., the transmitter). The current produces an alternating magnetic field which, in turn, induces voltages and current flow in the subsurface as a function of EC (Figure 3). Currents in the subsurface produce additional magnetic fields that are measured in the second antenna coil (i.e., the receiver). Based on the measured field and knowledge of the primary field, the EC of subsurface materials can be calculated. Using a range of frequencies and transmitter/receiver offsets or orientations provides information to spatially resolve subsurface EC structure.

Both the depth of investigation (DOI) for EMI and the resolution attained depend on the instrument's operating frequencies, the inter-coil spacing(s) and relative orientations, and the EC of the earth materials (Huang, 2005; Brosten et al., 2011). Data collected at larger inter-coil spacing or with lower frequency signals sample larger volumes of the earth at lower spatial resolutions, and are thus sensitive to deeper, broader structures. Conversely, data collected with smaller inter-coil spacing or higher frequency signals sample over smaller volumes and better resolve near-surface EC variations. DOI is also a function of the EC of soil or rock, with more signal decay in materials of higher EC.

Multi-frequency EMI data can be inverted to produce 2D cross sections or 3D volumes of subsurface EC (e.g., Brosten et al., 2011); however, it is more common to plot data for a single frequency or subset of frequencies or convert multi-frequency data to "total electrical conductivity" for interpretation. In this project, where the focus is instrumentation and rapid processing, we simply visualize the raw EMI data.

In principle, UAS-based EMI can allow for fully airborne (i.e., airborne Tx and Rx) or semi-airborne (i.e., ground-based Tx, airborne Rx) configurations. Deeper investigations may require more powerful and heavy Tx, precluding fully airborne surveys. In these cases, the Tx may be ground-based and moved by field operators or ground vehicles, or it could be carried by drones and thus 'hop' between locations. In this work, we consider only a single Rx, but our technology allows for 'swarms' of Rx antennas flying in concert around an airborne or ground-based transmitter. Swarms of Rx antennas would offer information-rich (allowing clear image construction), 3D datasets enabling higher resolution than can be practically achieved with existing ground-based EMI systems.

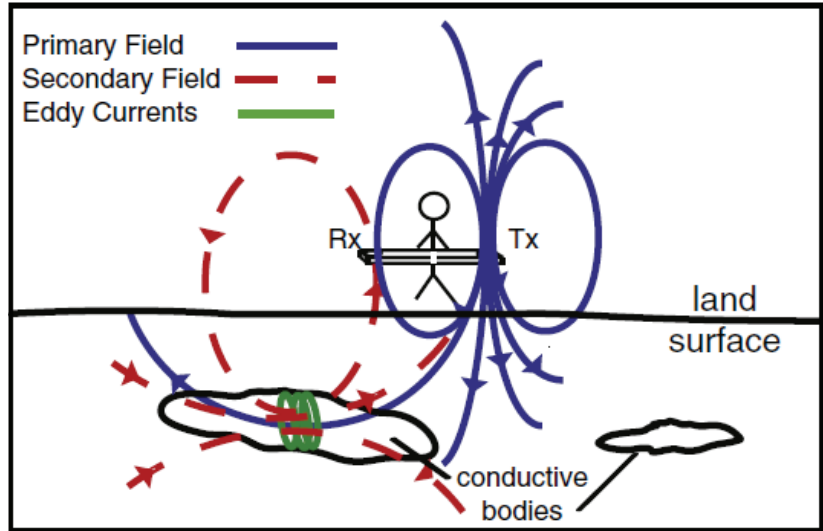


Figure 3. Schematic of the operation of a horizontal coplanar frequency domain electromagnetic system.

3.0 Approach

The systems used in this project were developed largely in house. This path was chosen in order to maintain control over the developed technology, both in terms of capability and security. The complete operation of the platforms developed and electronics contained therein, as well as the software that was written and implemented, was fully understood at a fundamental level by the team's engineers. The result was the successful development, demonstration, and full possession of a new 'blue technology' vector. Coils were wound by hand, important pros and cons being recognized along the way. Driver electronics were developed in house from the bare component level up, allowing a clean understanding of requirements for present and future designs. Custom software was designed and developed to seamlessly integrate with the new geophysical instrumentation and ingest both geophysical data and data from the UAS (i.e., navigation, orientation, etc.). The software leveraged existing PNNL Visual Sample Plan (VSP) code base which includes functionality for visualization and statistical analysis; this allows for field operators to gain real-time insight into datasets as data are acquired.

Various OEM (Original Equipment Manufacturer) electronics modules were employed for simplicity's sake in both system platforms. However, these were also entirely understood and well partitioned. These included GPS (Global Positioning System) units and radio modules, instrumentation amplifier development kits (boards), as well as the main microcontroller module.

A consequence of the in-house approach was that a significant amount of development had to accompany the integration of the sensor platforms involved. At the outset, it was not clear what the best way was to wind a coil for geophysical applications. Nor was it clear how the Tx and Rx electronics were to synchronize without physical connection between platforms. Nor was it clear how to arrange the data stream coming from the system into the right form to be stored in the required open-source format file. None of us had done these things before. However, the team had the confidence and expertise to efficiently explore the requisite spaces in order to find optimum approaches.

The higher research content inherent in the adopted approach also meant that considerable time and resources had to be committed to this effort. As a result, roughly mid-way through the period of performance the project was rescope to move away from originally planned field testing with airborne drone-based platforms and towards ground-based systems, which tolerated less well packaged electronics and larger batteries, for example. A more open-frame construction was thus also appropriate. Therefore, the available resources were expended on demonstration of the new technology rather than the specific repackaging necessary for drone-based flight. The latter step was left for another project operating in parallel with this LDRD and beyond, which directly benefited from it (DOE-funded project "Drone-Based Geophysical Surveying and Real-Time AI/ML").

4.0 Detail

This LDRD project required significant R&D in two areas: (1) instrumentation (hardware), and (2) software, as detailed in sub sections below. That said, there is also some software/firmware development that occurred which was part of the hardware. This includes code that runs on the microcontrollers on the actual platforms themselves, as distinct from software written for execution on a laptop to process data.

4.1 Instrumentation Hardware

In conventional EMI instrumentation (e.g., Figure 2), physical connections between Tx and Rx units readily allow for precise timing of signal transmission and reception using shared electronics for a common timing system. Although this ‘umbilical’ has posed no significant disadvantages to the standard practice of EMI, it is highly problematic for drone-based deployments. Overcoming this limitation was a major thrust of the LDRD. To this end, the team developed two independent platforms for this demonstration, one for transmission and the other for measurement. As outlined above, custom analog and digital electronics subsystems were developed for each platform. The Tx platform also served as the “base” in that the laptop used in the system, serving as the operations and data center, connected directly to the Tx platform, which was physically stationary in this system. The Rx, also known as the “rover,” was mounted on a platform with wheels. It reported information via radio link to the transmitter, or base.

Since both platforms needed to best expose their respective coils (antennas) for interaction with each other at considerable distance (tens of meters), with minimal interference (except by metallic objects we may wish to detect), the use of metal was minimized in the construction of these platforms. To this end, plywood sheets were used as the basic structure, with plastic hardware for securing subassemblies. Since these platforms were relatively large, the electronics were mounted on smaller plywood boards in each case, which could be easily removed and worked on during development and lab testing.

When two coil-based antennas of this kind couple together as in this demonstration, the received signal by one from the other falls off as one over separation distance cubed ($1/d^3$). This presents one of the principal challenges with the idea of separating transmitter and receiver – providing adequate drive and receiving adequate signal strength. This implies that the transmitter has to be powerful, and the receiver has to be sensitive. Thus, in the transmitter, a high-power drive amplifier is required. In the receiver, a sensitive differential instrumentation amplifier (IN AMP) is required to achieve good signal to noise ratio. (An additional practicality is that this IN AMP also needs to be able to reduce its gain when the platforms are in close proximity (to avoid overload conditions) and increase it when further apart (to retain sensitivity).)

Furthermore, under these signal constraints it’s difficult to achieve good coupling using just the bare reactance of such coils – it’s logistically difficult to drive a bare Tx coil hard enough because its inductive reactance gets in the way. In a complementary way, a receiver using a bare coil develops relatively little voltage in response to a magnetic signal because of the same phenomenon, but in the opposite sense – the coil’s impedance is now too low. To overcome these problems, both the Tx and Rx drive systems in this project use *resonant* systems to optimize the performance in each case: the current is maximized in the transmitter and the observed electromotive force (EMF) is maximized in the receiver. Resonating the selected coils with appropriate capacitors was a significant part of the electronics R&D for this project. (Further explanation of resonances can be found in Chapter 6 of the ARRL Handbook,

published by the National Association for Amateur Radio, and many books on basic electronics.)

In general, surveys done with instruments of this kind, regardless of Tx/Rx configuration, are conducted over a range of frequencies in order to facilitate geophysical inversion in order to produce an image. Indeed, commercial units operate over a considerable frequency range, typically below 100 Hz out to 100 kHz or more (Huang, 2005). However, due to limited resources, only one operating frequency was chosen for this particular demonstration, namely 3 kHz (3.052 kHz in actuality, due to signal generation constraints). This restriction avoided the need for complex switching systems on both Tx and Rx platforms, while still allowing demonstration of the capability, both hardware and software.

A discussion of each platform is given in the subsections below. Several items common to both platforms will be discussed in more detail in a separate subsection thereafter.

4.1.1 Receiver (Rover)

A photograph of the rover is shown to the left in Figure 4. This platform (24 by 48 inches) was mobile in that it sported large plastic wheels allowing it to be pulled back and forth across the field test site using two long lengths of rope. This was a far cheaper and a more expedient option for the demonstration of the new technology than performing the deeper electronics development necessary for drone-based flight. To the right in the figure, is shown all the components that make up the Rx electronics subassembly. This includes a GPS unit (shown along with its antenna), a digital synthesizer board (DDS), a precision MEMS-based clock (CLK), an RS-422 digital comms unit (422), and a radio (RADIO) used to communicate with the transmitter platform. The large north-south oriented circuit board shown in the middle is a signal processing board leveraged from a previous LDRD/Agile project, namely INSITE (Peripheral node). (INSITE stands for the PNNL Agile LDRD investment entitled Induced Spectral Imaging Technology for the Environment.) This board contains an analog-to-digital converter (ADC), electrical isolators and the NetBurner microcontroller unit, which is used to compute signal amplitude real and imaginary components, incorporate GPS data, and manage data flow and communications.

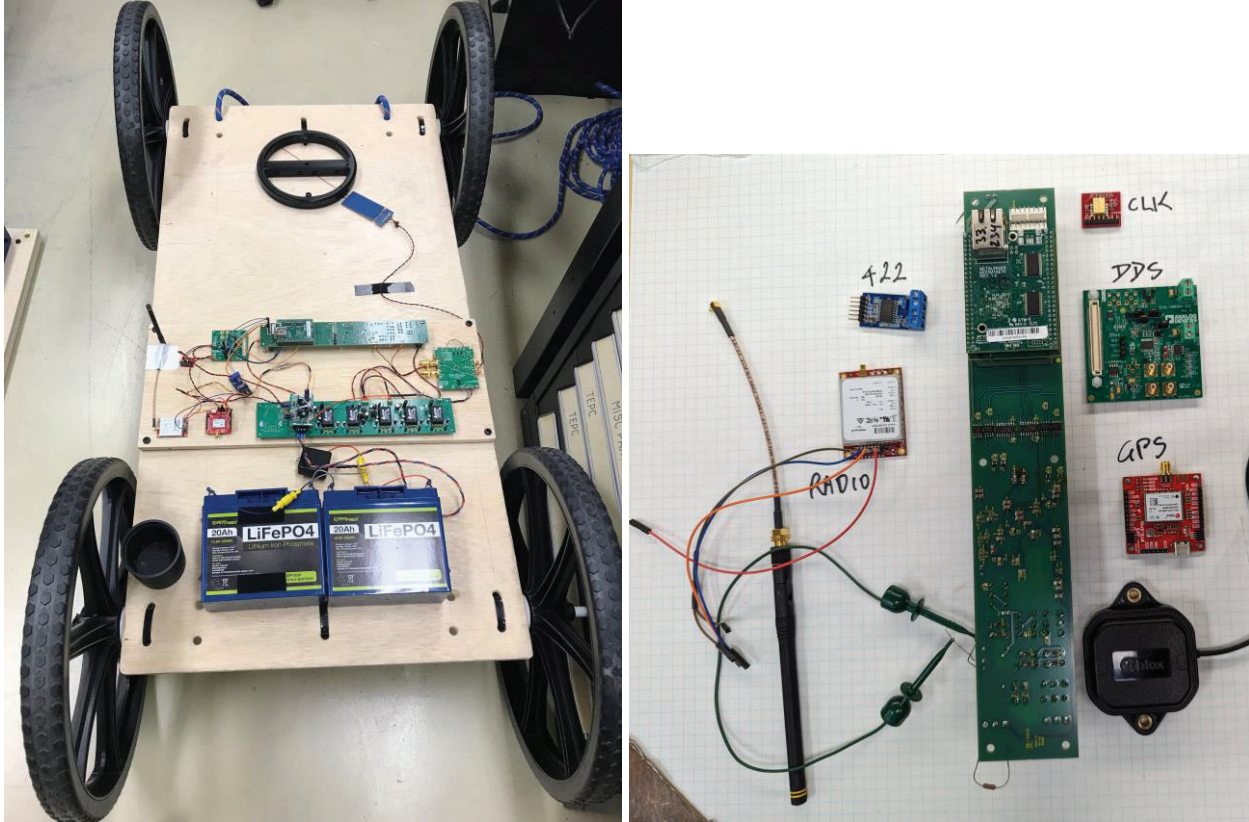


Figure 4. Left shows a picture of the receiver platform (rover) taken before field testing. The platform is a 24- by 48-inch by 5/8-inch thick sheet of plywood, with subcomponents attached using plastic hardware. Moving from the top of the figure down to the bottom are seen the receiver coil (aka antenna), the receiver electronics board, and finally the batteries. Right shows a photo of all the subelements of the electronics board before assembly, including the radio, RS-422 digital adapter (422), INSITE analog to digital / microcontroller board, precision clock (CLK), digital synthesizer (DDS), and GPS.

Missing from this photo of the Rx electronics is a second precision IN AMP, in addition to the one that was already on the INSITE peripheral node board. This amplifier module is seen on the electronics subassembly board seen in the left-hand frame of the figure. It's the green circuit board on the right-hand side and is in fact an LTC6373 development/evaluation kit. (The IN AMP on the INSITE board is also of this kind).

The operation of this platform is illustrated in Figure 5, and is as follows. Signals from the coil at the desired operating frequency (3 kHz) are preferentially selected by the resonance of the coil and a parallel capacitor (mounted on the small blue circuit board next to the coil). These signals are passed to the precision instrumentation amplifier (IN AMP) (LTC6373 dev. kit discussed above). The output from the IN AMP is passed to the ADC on the INSITE board, thence the NetBurner via electrical isolators. We now have a digitized version of the received signal waveform.

In parallel with this, the DDS produces a low-jitter sampling pulse train to trigger the ADC at precise points in time, allowing a similar system on the transmitter platform to correlate with this process and effectively preserve phase information between the two platforms. This process is achieved through use of the precision the 25-MHz MEMS clock, which is accurate to 5 parts per billion (5 ppb). This unit is also relatively immune to physical vibration, making it perfect for future drone-based use. It's also temperature controlled using an onboard oven inside the chip.

In this way, the use of two such clocks allows the two platforms to perform phase measurements without a physical umbilical connecting the two.

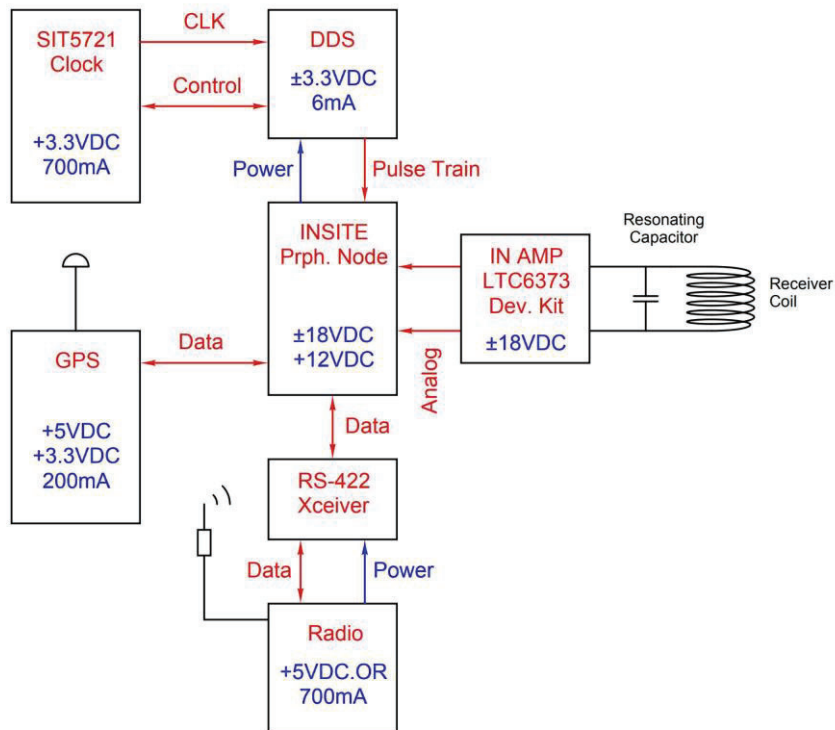


Figure 5. Block diagram of receiver platform. This shows interconnections as well as DC power requirements.

In addition, the onboard GPS system gives time-stamped GPS coordinates, which are also included in the data packet sent to the Tx platform via the NetBurner and thence radio unit, for acquisition, storage and processing (via laptop computer).

Since a lot of work went into the winding and testing of coils, special mention of the details is made here. The receiver coil was an 8-inch 3-D printed unit, wound with 18-AWG magnet wire. The process of winding it along with the finished product is shown in Figure 6. One of the problems with winding effective coils for this and similar purposes is to keep the self-resonance of the coil at as high a frequency as possible. This is because the coil cannot be used effectively for the intended purposes at frequencies above this, because the effective current doesn't flow through the inductance of the coil, but rather directly through the interwinding capacitance. Thus, the effective interwinding capacitance must be kept to a minimum. This requires a regular tidy coil winding cross section, with minimal incidence of breakthrough from one layer to more than one below it. It turned out this was harder than imagined to achieve. It took some practice!



Figure 6. Left shows the winding process of the receiver coil former using AWG18 enameled copper wire. Care had to be taken to pack the turns in carefully so that wires from adjacent layers didn't come close to one another. Right shows the finished receiver coil. The coil has an inductance of 2.67 millihenries, a DC resistance of 1.09 Ω , and a self-resonance of 298.5 kHz.

Figure 7 shows the impedance analyzer response of the finished receiver coil to contain a self-resonance at 298.5 kHz. Effective operation must be below this frequency, and well so for good signal to noise ratio. This coil formed an excellent receiver at 3 kHz. (As an aside, for readers' edification of the importance of this winding process and analysis, coils similar to this one have formed effective Rx antennas at 100 kHz in other projects. But they did not serve effectively as Tx coils, the resistive part of the impedance being too high.)

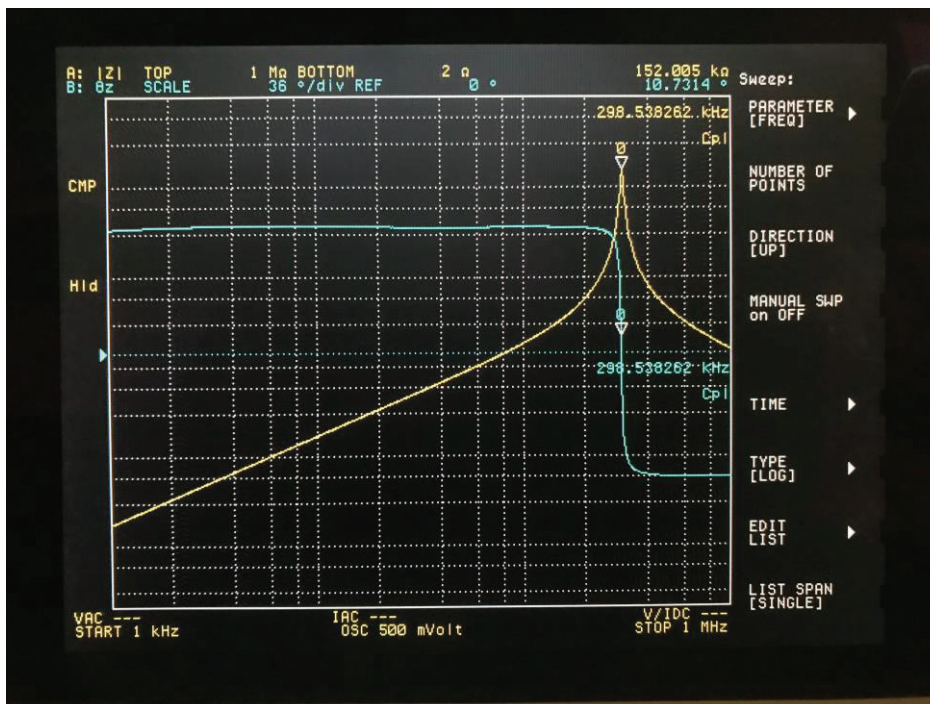


Figure 7. Impedance analyzer response of finished receiver coil showing a self-resonance of 298.5 kHz.

The final Rx coil characteristics include: 82.5 turns of 18-AWG wire; inductance of 2.67 milliHenrys (mH); DC resistance of 1.09 Ω ; self-resonance of 298.5 kHz. This implies an effective self-resonating capacitance of 106.5 pF (note, this isn't a *real* capacitance, but an

'effective' one). Resonating this coil at 3.052 kHz required a capacitance of 1.018 μF . Accommodating the effective self-capacitance of the coil, we found that a 1 μF orange drop capacitor worked just fine.

4.1.2 Transmitter (Base)

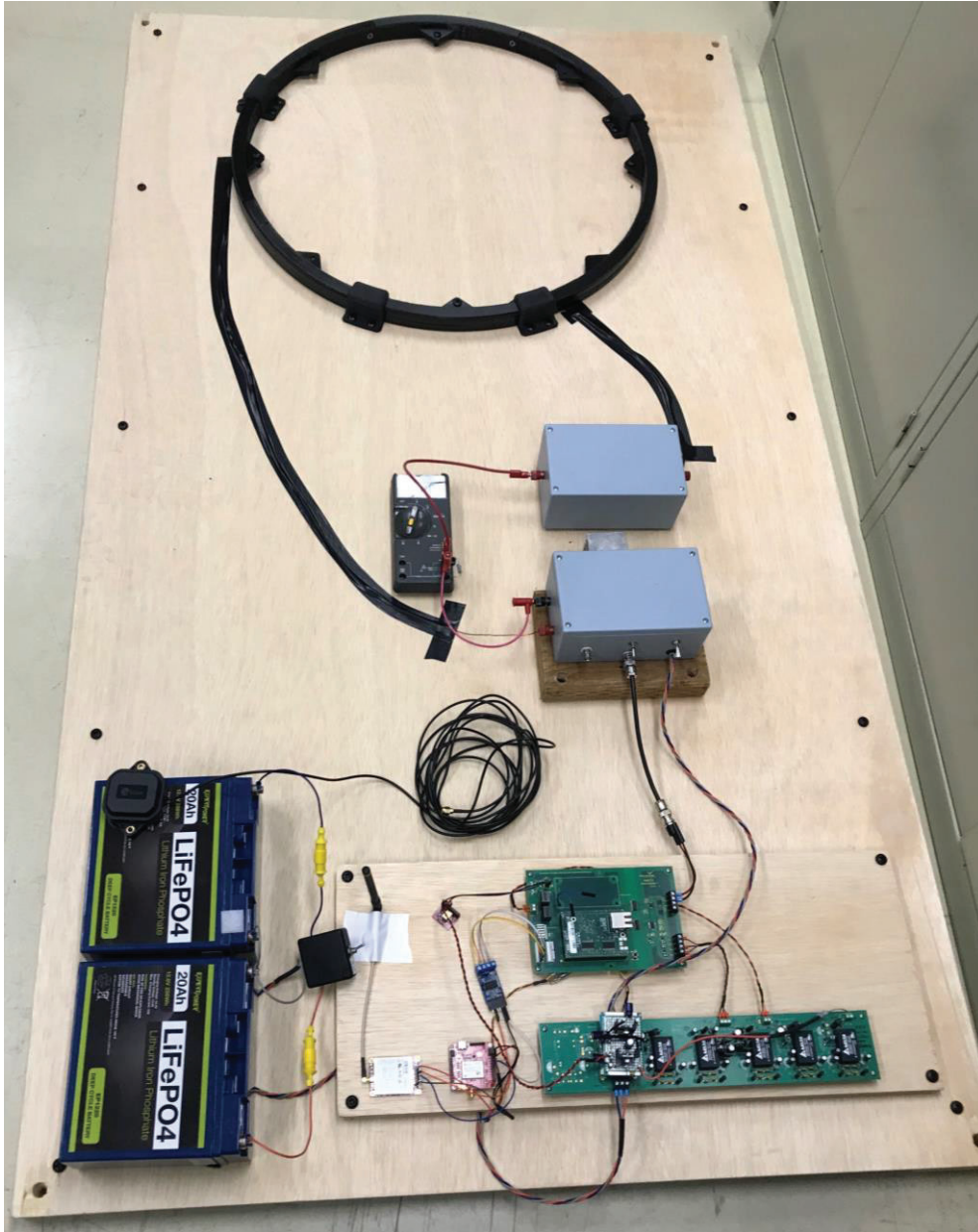


Figure 8. Photograph of the Tx platform (base) taken before field testing. The platform is a 38- by 68-inch by 5/8-inch thick sheet of plywood, with subcomponents attached using plastic hardware. Moving from the top of the figure down to the bottom are seen the Tx coil (aka antenna), the resonating capacitor unit and power amplifier (gray boxes), current sensing meter, signal generation board (INSITE intermediate node board) and batteries.

A photograph of the Tx (base) is shown in Figure 8. This platform (38 by 68 inches) was stationary during the field test, thus serving as a base for the system. The laptop used to control the system was connected directly to the electronics board of this platform via Ethernet cable. Moving from the top of the figure down to the bottom are seen the Tx coil (aka antenna), the resonating capacitor unit and power amplifier (gray boxes), current measurement meter, signal generation board and batteries.

The operation of the Tx electronics is illustrated in Figure 9. The Tx electronics synthesized a precision 3.052-kHz sinusoidal waveform using another circuit board borrowed from INSITE (INSITE Int. Node), informed once again by a precision MEMS clock (SIT5721). This signal is passed to the power amplifier, thence resonated coil. Signals received from the Rx platform (including GPS information) via the radio unit and the RS-422 transceiver were combined with information from the Tx (including its own GPS information) to form the final data packet stream passed to the laptop (connection not shown).

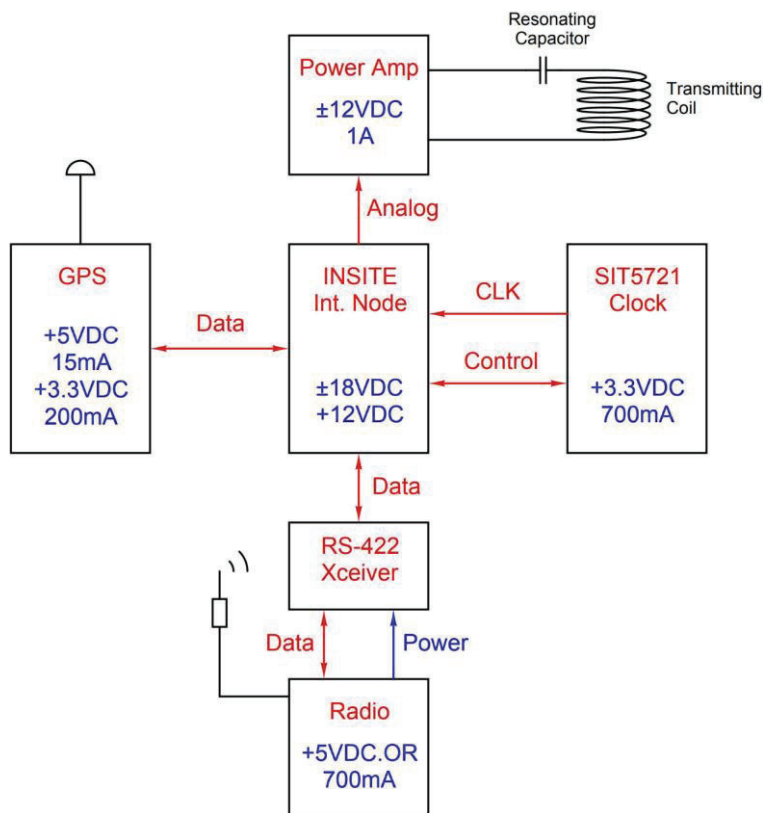


Figure 9. Block diagram of transmitter platform. This shows interconnections as well as DC power requirements.

The coil for the Tx was actually the first coil that we wound, and in some ways it was the most demanding because of its size. It was 24 inches in diameter and didn't have 3D printed cross members. As a result, a disk structure had to be used to support the coil during the winding process. A photo of the winding process is shown in Figure 10. 81 turns were wound onto this coil out of an expected maximum of 100, with much care being taken to avoid slip-downs of turns penetrating previous layers, as this tends to greatly reduce the usability of the coil at higher frequencies as explained previously.

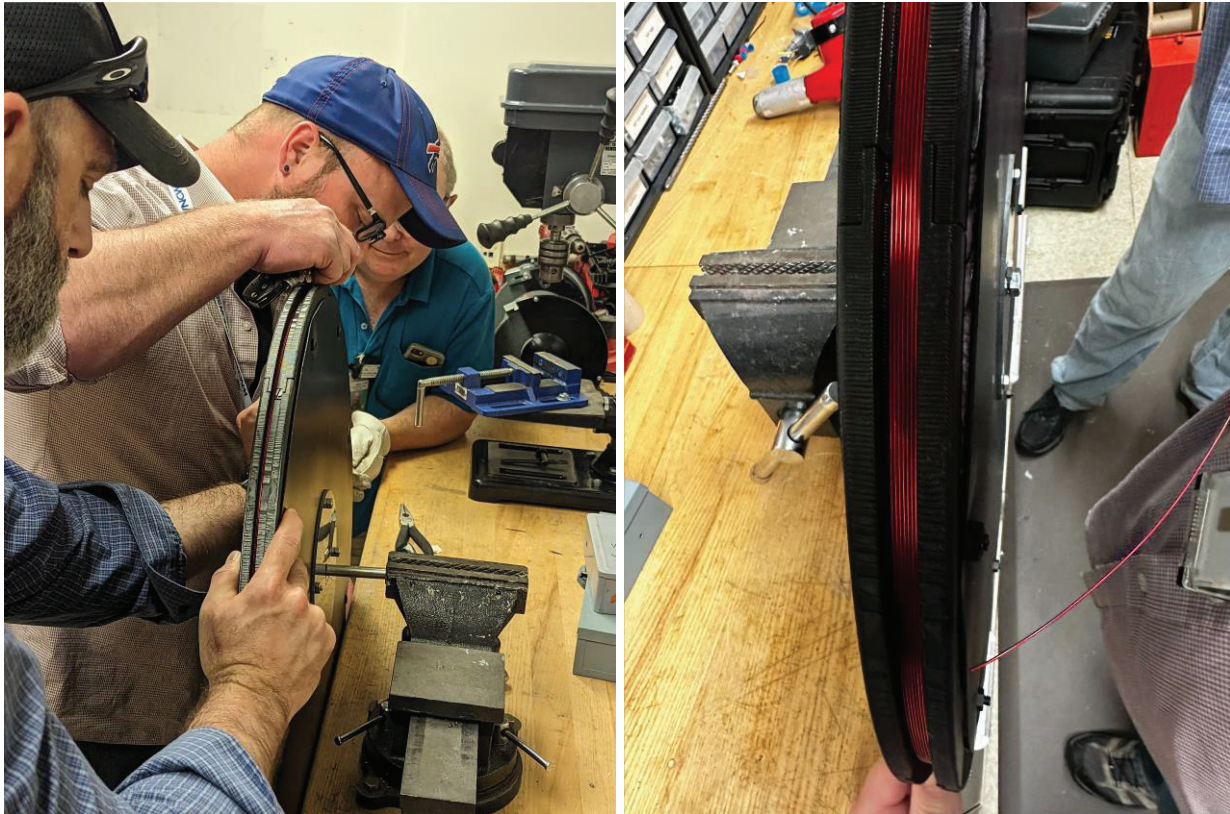


Figure 10. Photographs showing the process of winding the 24-inch Tx coil. Large plastic disks had to be used to support the open-frame coil during this process. 81.3 turns were wound out of an expected 100, of 18-AWG wire.

Figure 11 shows the impedance analyzer response of the finished Tx coil to contain a self-resonance at 90.83 kHz. As with the Rx coil, effective operation must be below this frequency. However, this turns out to be more stringent in this case, and operation in fact must be well below this frequency. This is because the Tx coil is resonated in series, not parallel, and correct operation depends on a low ohmic (real part) of the impedance upon resonance. By comparison, the parallel resonance of the Rx system operates at a high impedance point, and a little more real impedance doesn't matter. What's odd, is that not all this real impedance term comes from actual DC resistance, but rather, seems to manifest itself as other loss terms related to finite Q-value. Surmounting this in our demonstration would have required much larger drive voltages and unnecessary heating of components. Q-values, in general, climbed as test frequencies increased. At high values it became impractical to resonate the coil precisely at the narrow resonances produced. This is in part why a relatively low operating frequency of 3 kHz was chosen, although the coil could have operated comfortably up to about 10 kHz.

Aside: This is a complex issue, and it's difficult to fully understand or explain. Delving deeper into it was also beyond the scope of this project. Nevertheless, omission of it would be a disservice to ourselves in the future. The bottom line is that there is more to understand about series resonances in high-power drive coils.

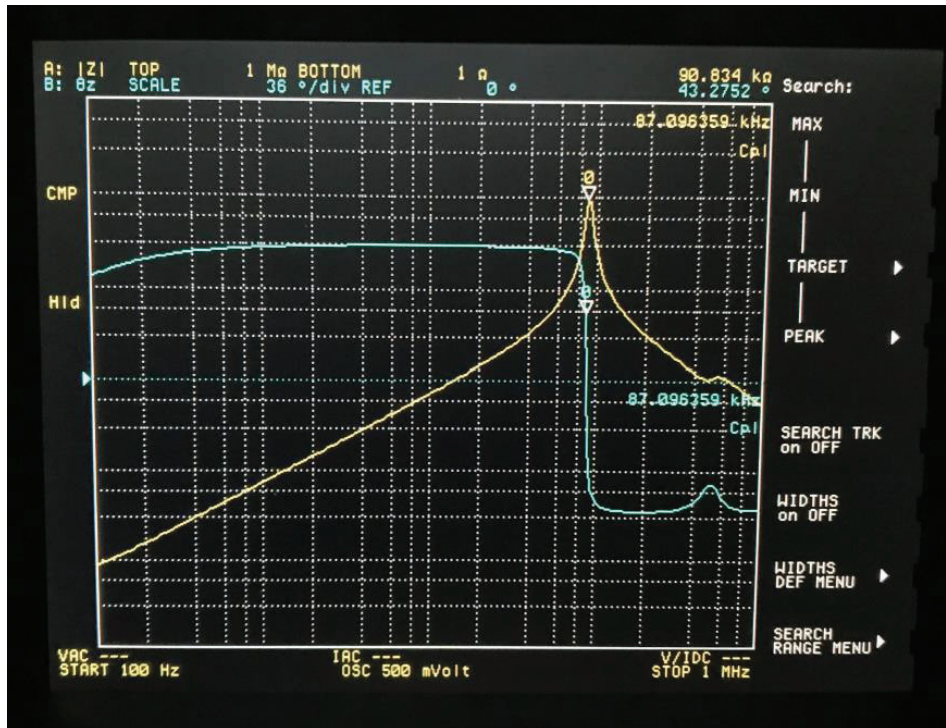


Figure 11. Impedance analyzer response of finished transmitter coil showing a self-resonance of 90.83 kHz.

The final Rx coil characteristics include: 81.3 turns of 18-AWG wire; inductance of 11.27 milliHenreys (mH); DC resistance of 3.45 Ω ; self-resonance of 90.83 kHz. This implies an effective self-resonating capacitance of 272.4 pF (note, this isn't a *real* capacitance, but an 'effective' one). Resonating this coil at 3 kHz required a capacitance of 249.5 nF.



Figure 12. Photo of the capacitor box used to resonate the Tx coil. This consists of three parallel banks of caps, each consisting of a series string of two. Two of these strings comprise 220-nF caps, while the smaller central one comprises 47-nF caps. This gives a total capacitance of 243.5 nF.

Figure 12 shows the capacitor box used to resonate the Tx coil. Contained within is a non-copper circuit board supporting three parallel banks of capacitors, ultimately connected to

banana plug jacks on the outside of the box. Each of the three capacitor banks consisted of a series string of two capacitors. Two of these comprised 220-nF caps, while the smaller central one comprises 47-nF caps. This gives a total capacitance of 243.5 nF. This configuration was necessary because series resonances of coils can result in quite high voltages, sometimes up to 300V peak. Since the ratings of the capacitors (600V) is a DC rating, and typical AC ratings are around 250V, multiple series capacitors are required to prevent failure. (It should also be noted that the AC ratings are only for 60 Hz. Stress on capacitors is much worse at higher frequencies, like 3 kHz.)

Aside: It should be pointed out that potentials achieved during this project fell under minimal risk because there was well less than 5mA supporting it. To wit, the energy available in a series resonance as described is only equal to the maximum contained with the resonating capacitors, which at 300V, for example, is 11 mJ for this total capacitance. (The threshold for high risk electrical is 1 J.) In addition, no points of voltage in excess of 24V were accessible to the user.

4.1.3 Common Elements

Batteries

The batteries chosen as power sources for both Tx and Rx platforms were of the lithium iron phosphate (LiFePO₄) chemistry. These are very robust, safe, high capacity and most importantly light-weight batteries. This made them an ideal choice for this first demonstration of this technology, even though they are relatively large compared to other choices, such as lithium-ion chemistry. Space and size were not tightly constrained as can be seen in the photos of the platforms discussed previously. Had drone-based flight been pursued, this would have been a problem, and more compact lithium-ion batteries would have had to have been used, requiring more care and presenting more risk.

Operational Software

Both platforms used a NetBurner MODM7AE70 system-on-module (SOM). This is a very convenient unit allowing processing and comms in an accessible and convenient manner. To wit, the receiver firmware programmed onto the NetBurner on the Rx platform processes received signal waveforms to compute a cartesian phasor representation of the received signal. The results are then combined with position and time information provided by the GPS module to form Rx data packets, which are then transmitted over radio to the Transmitter (or ground station) for further analysis.

4.2 Software

In standard EMI practice, data are collected and quality-checked in the field, but rarely are data fully worked up until after completion of a field campaign. This practice has been judged to be cost-effective in the past. For ground-based surveys, it has been cost-effective to focus labor on data collection while staff are still in the field. In the case of airborne surveys, there is little opportunity to adapt survey designs while data is being collected, and data analysis can take weeks given the size of datasets. We contend, however, that a new paradigm will emerge concomitant with the operationalization of drone technology. With the increasing automation of data acquisition and the emergence of AI for autonomous data analysis and interpretation, we predict increasing interest in real-time analysis, real-time interpretation, and adaptive surveying

in which data acquisition will be adjusted to optimize survey parameters, reduce uncertainty, and achieve data quality objectives. Toward this end, in this LDRD project we sought to lay the groundwork for real-time drone-based EMI.

Software developed in this project included python code for data acquisition, data management, and real-time visualization of raw and processed data. This work leveraged the existing code base of PNNL’s VSP software. The HDF5 database format was adopted for data management. A graphical user interface (GUI) was developed (Figure 13) using the Kivy package in Python, providing the user with a straightforward means of initializing the HDF5 file with user-inputted metadata, establishing a data connection between the field laptop and the instrument using the Transmission Control Protocol (TCP), and parsing data packets into data arrays that can be processed in small chunks and viewed in real-time. Packaging the code into a GUI also ensures that the various components of the software work together seamlessly. The GUI includes a plotting tab that populates map-view plots of raw and processed data as the sensor moves through the survey area. Removal of the primary field to isolate the induced field (Figure 15) is done geometrically using data from orientation sensors on the loops to correct for tilting of the magnetic field created by the Tx and for the change in vertical flux caused by tilting of the Rx, as well as real-time kinematic GPS for relative positional accuracy within centimeters. Orientation and position information are updated 10 times per second to ensure accurate removal of the primary field with every data sample.

The use of the HDF5 format allows for all of the information for a project to be stored in a single file. Data are organized in a hierarchy (Figure 14) of various zones within each project, different surveys within each zone, and individual flights within each survey. Parameters related to the sensors and drones are also saved. HDF5 is a flexible format that allows for expansion if future needs are identified. The format is widely used across many industries, with many existing software libraries designed to quickly access the data on any platform, whether on a local machine or in cloud-based processing.

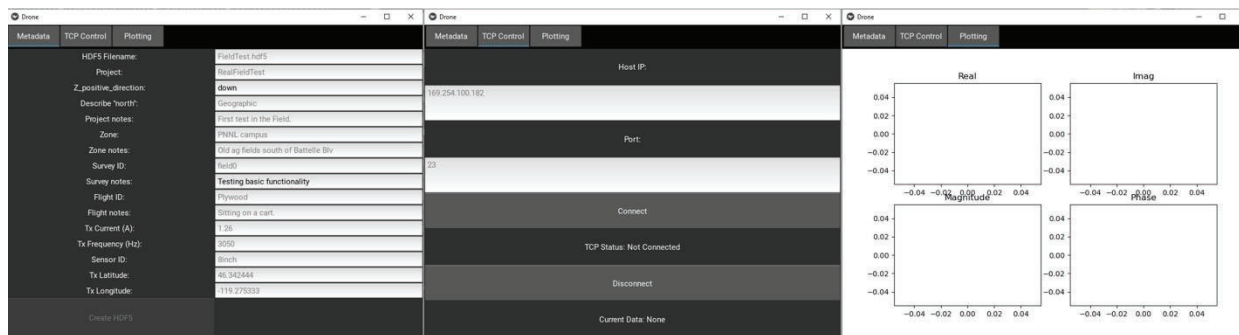


Figure 13. Screen capture of the GUI for measurement acquisition and control and real-time visualization of data in the field.

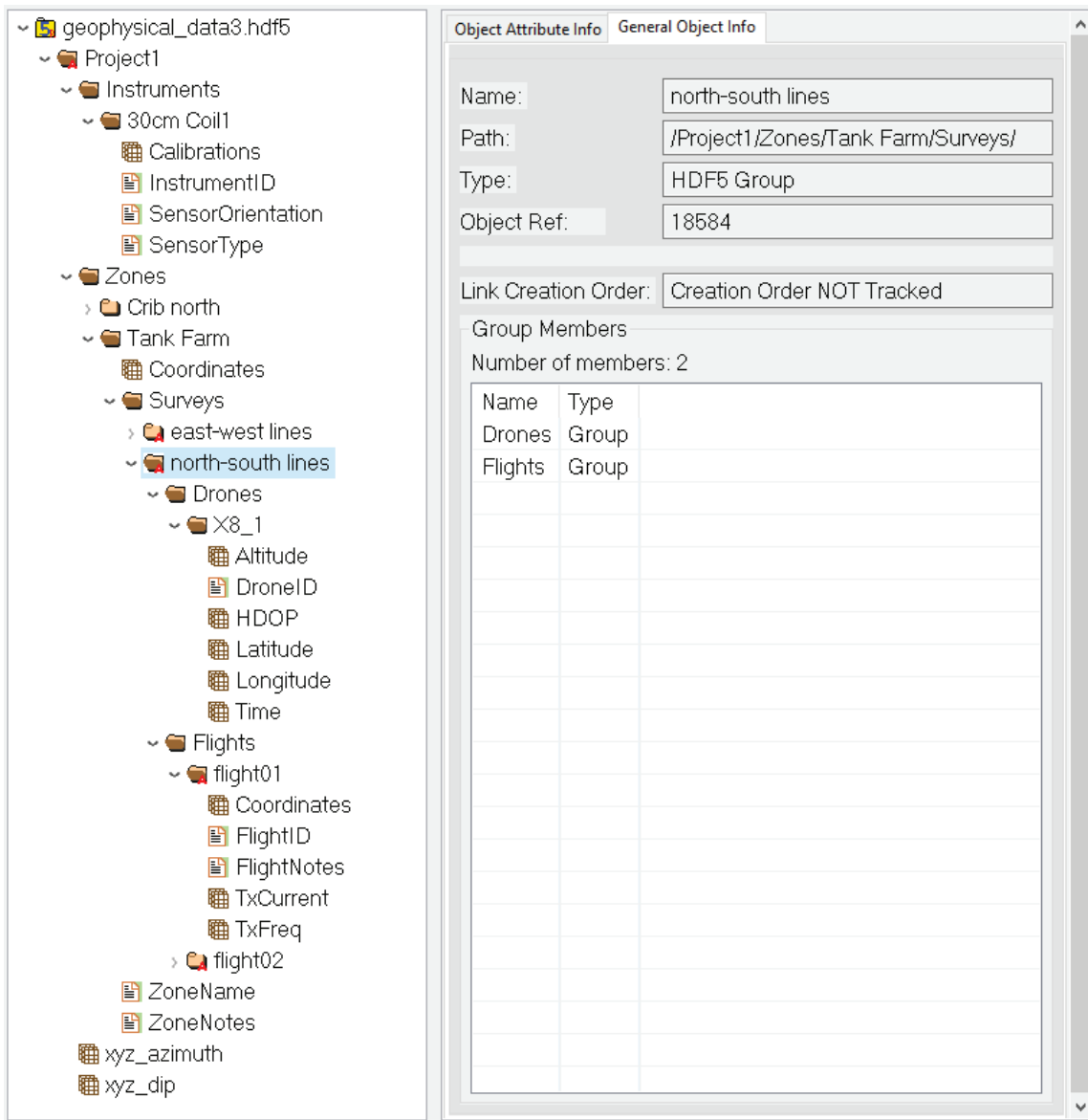


Figure 14. Screen capture of the digital object description for the HDF5 database in which the drone data are organized.

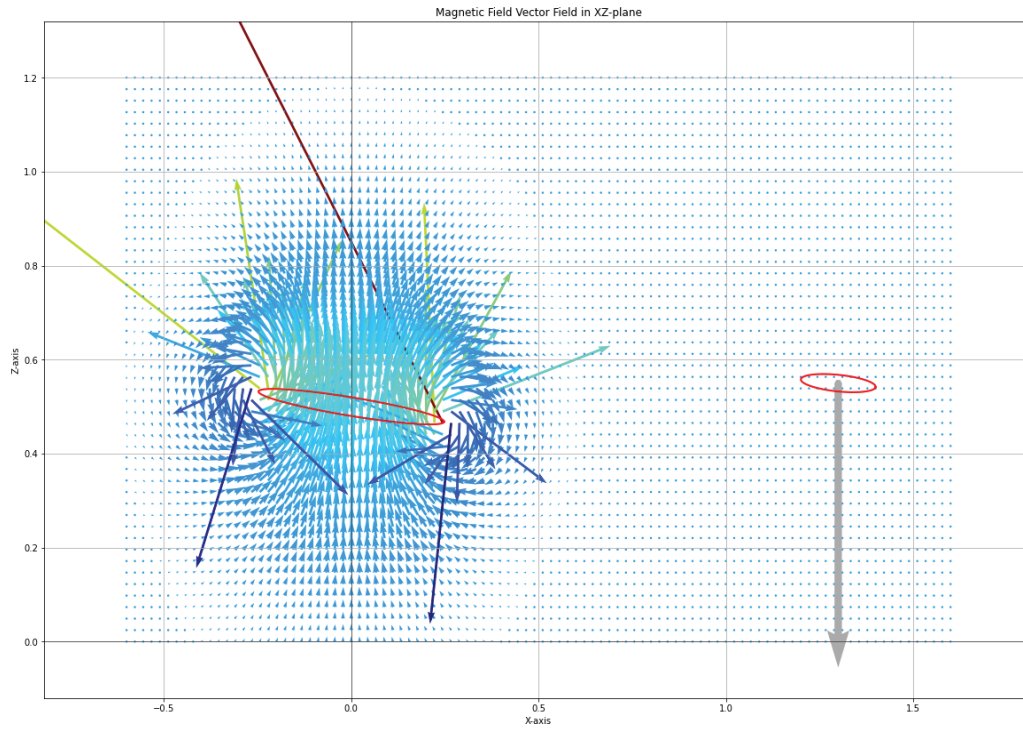


Figure 15. Analytical modeling result showing the transmitter coil, generated primary magnetic field, and receiver coil measuring this.

5.0 Field demonstration

A field demonstration on the PNNL campus was conducted in December 2023 to test the new hardware and software components in realistic conditions. Given fiscal limitations and practical constraints on flying the prototype components, which were at the time yet to be miniaturized, a ground-based demonstration was conducted instead, as explained in Section 3.0. The custom base and rover designed and fabricated for this purpose (discussed in Section 4.0) are shown ready for the field test in Figure 16.

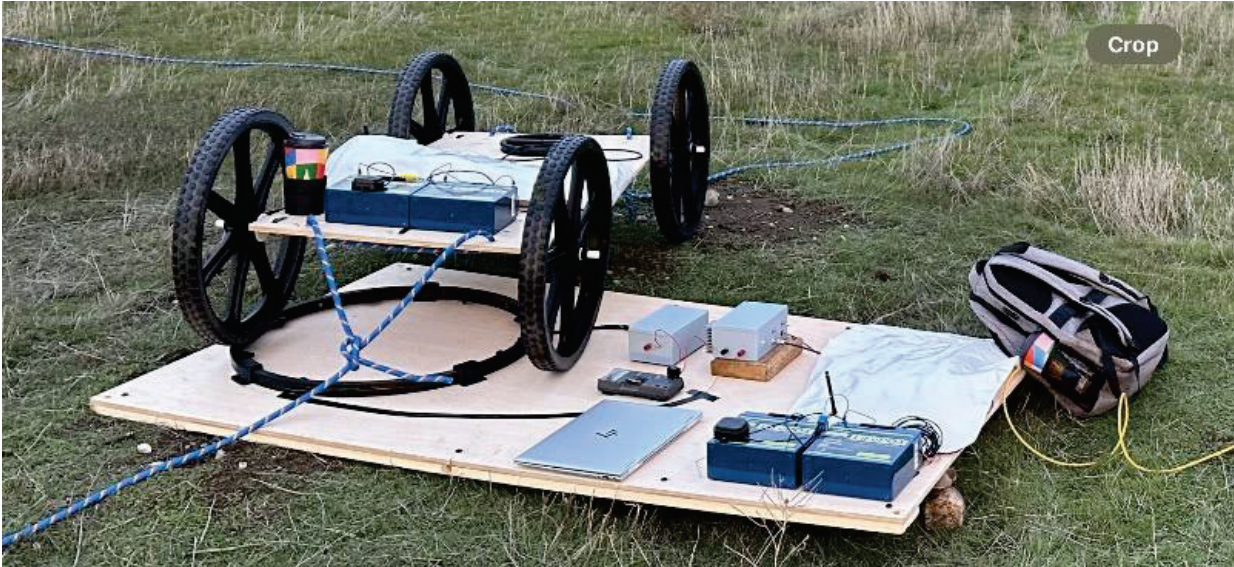


Figure 16. Photograph of field test setup, showing transmitter (larger black coil), roving receiver cart and coil, field laptop, and electronics.

The test site was an open field at the southern end of the PNNL campus, in Richland, WA (Figure 17). Two metal targets (i.e., jacketed extension cords) were placed in the study area. Using ropes secured to the front and back of the cart, PNNL staff pulled the receiver across the study site.

Figure 17. Photograph of field test site, the "south field" at the southern end of the PNNL campus.

Using a field laptop, scientists controlled the acquisition of EMI measurements. Data were continuously transmitted via radio link to the laptop for integration into the HDF5 database, along with GPS information for the rover position. The raw data, displayed as real and imaginary components (**Error! Reference source not found.**), clearly show the effect of the metallic targets, as well as the dominant effect of the primary field generated by the transmitter.

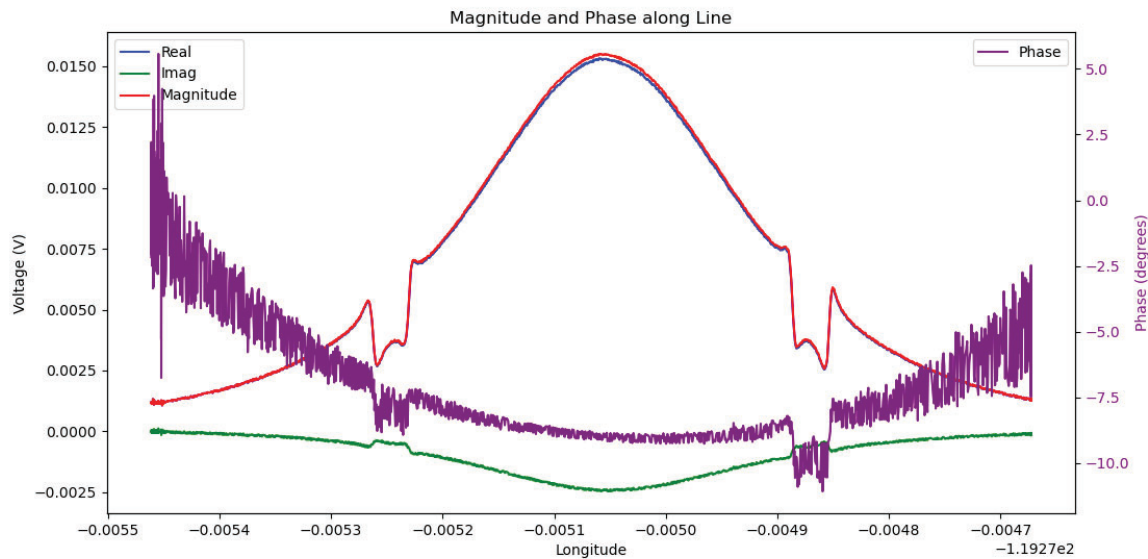


Figure 18. Raw EMI data collected in the field test, displayed. The Tx was located midway along the transect, where magnitude is greatest. The effect of two metallic targets is clearly visible.

Notably, this information was processed and visualized in real-time, with user-friendly displays of data to field operators on the field laptop. This is depicted in Figure 19, which shows all relevant aspects and equipment of the entire process.

Using the analytical modeling code described in Section 4.2, the effect of primary field was effectively removed from the data, as shown in Figure 20. Qualitatively, the raw data appear cleaner than GEM-2 data collected as part of the field demonstration (**Error! Reference source not found.**).

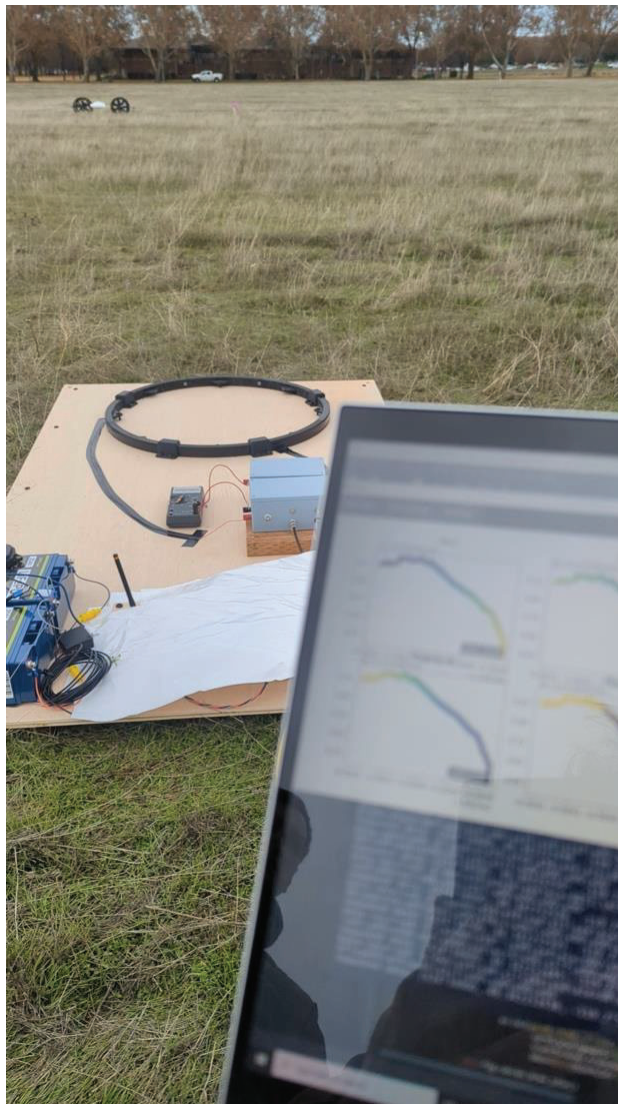


Figure 19. Photograph of field test, with field laptop in the foreground, showing the GUI, Tx in the middle ground, and roving Rx cart in the background.

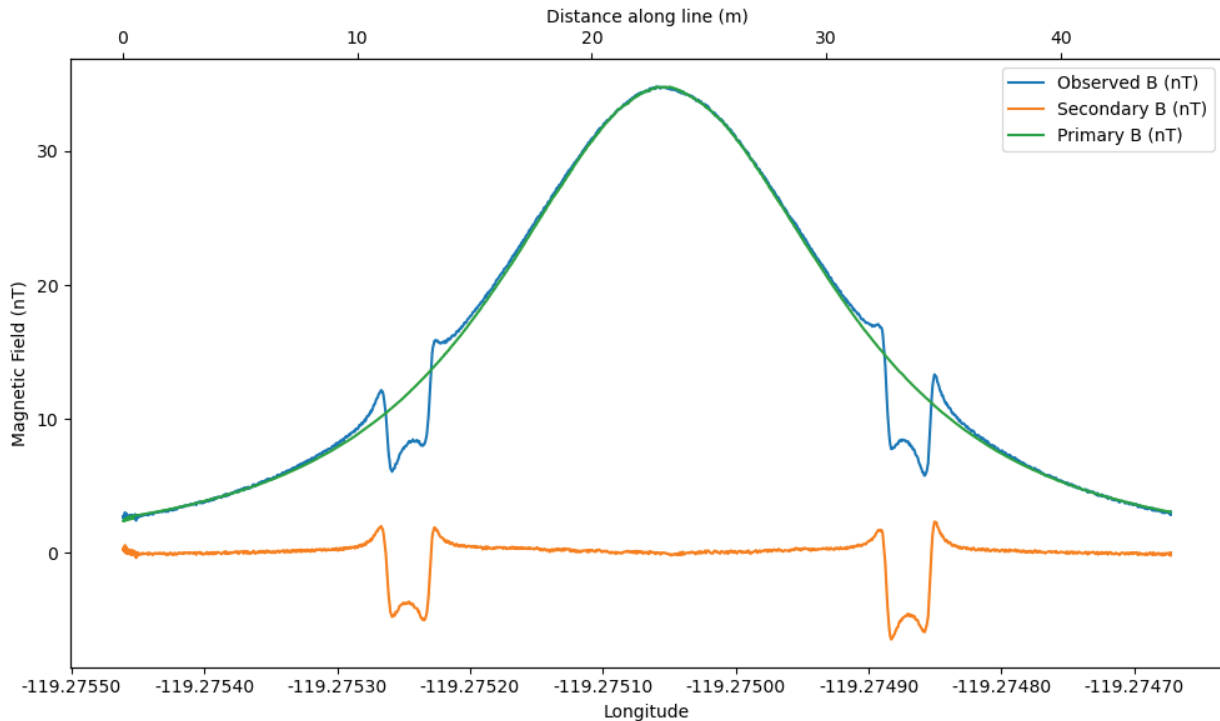


Figure 20. Observed EMI data collected in the field test (blue) and data corrected (orange) to remove the effect of the primary field (green) using the analytical model.

In summary, the major takeaways from the field demonstration are:

1. The new Tx, Rx, and measurement control instrumentation were successfully field-tested and produced clean data that clearly showed the presence of the metallic targets;
2. The software for measurement control, data management, and data processing was successfully field-tested and performed as designed, providing real-time delivery of results to end users; and
3. The model-based removal of the primary field from the measurements was effective for this dataset.

6.0 Discussion & Conclusions

The frequency-domain EMI geophysical method is particularly well suited to deployment on airborne platforms (e.g., UAS), as it requires no contact with the ground and allows for multi-scale characterization. In principle, EMI receivers could be deployed on swarms of UAS, with receivers on multiple UAS and a single transmitter on a single UAS, which could be airborne, ground-based, or semi-airborne, moving by air from one ground location to another. In conventional, COTS (Commercially available off-the-shelf) EMI systems, however, transmitters and receivers are physically connected, thus constraining surveys to single-drone operations. Although drone technology presents enormous opportunities to enhance and automate the acquisition of EMI geophysical data, significant R&D is required to fully capitalize on all the capabilities that drones offer.

In this LDRD project, we conducted R&D to overcome the existing technological constraints for deployment of EMI instrumentation on drones. Through advancements in instrumentation and software, we successfully (1) designed, built, and field-tested custom EMI instrumentation in which the transmitter and receiver are physically independent, and (2) developed and tested software for real-time control of the hardware, data management, and data processing. The field test, although ground-based, highlighted the potential of EMI data acquisition from drone platforms and demonstrated the new hardware and software capabilities. To the best of our knowledge, this is the first demonstration of frequency-domain EMI with fully, physically independent transmitter and receiver units.

This LDRD project established a foundation for developing a drone geophysics capability at PNNL. The next steps toward this long-term goal include: (1) building capabilities for rapid 3D modeling and inversion that allows for complex 3D transmitter/receiver geometries, for fully airborne and semi-airborne configurations, (2) full-scale airborne field demonstrations, and (3) development and demonstration of multi-frequency instrumentation. Work is underway in a projected funded by the Department of Energy Minerals Sustainability Program (DOE-funded project “Drone-Based Geophysical Surveying and Real-Time AI/ML”), aimed at leveraging drone technology and geophysical imaging to support development of critical minerals from secondary resources and waste streams.

7.0 References

- Brosten, T.R., Day-Lewis, F.D., Schultz, G.M., Curtis, G.P., and Lane, J.W., Jr., 2011, Using frequency-domain electromagnetic surveys to characterize a former uranium mill site, Naturita, CO, *Journal of Applied Geophysics*, doi:10.1016/j.jappgeo.2011.02.004.
- Harvey, M. C., Hare, D. K., Hackman, A., Davenport, G., Haynes, A. B., Helton, A., et al. 2019. Evaluation of stream and wetland restoration using UAS-based thermal infrared mapping. *Water* 11 (8), 1568. doi:10.3390/w11081568.
- Huang, H., 2005. Depth investigation for small broadband electromagnetic sensors. *Geophysics* 70 (6), G135–G142.
- Jaysaval, Daniil V. Shantsev, Sébastien de la Kethulle de Ryhove, Efficient 3-D controlled-source electromagnetic modelling using an exponential finite-difference method, *Geophysical Journal International*, Volume 203, Issue 3, December 2015, Pages 1541–1574, <https://doi.org/10.1093/gji/ggv377>
- Jaysaval, P., Shantsev, D., de La Kethulle de Ryhove, S., 2014, Fast multimodel finite-difference controlled-source electromagnetic simulations based on a schur complement approach. *Geophysics*, 79, E315-E327 <https://doi.org/10.1190/geo2014-0043.1>.
- Johnson, T.C., Strickland, C., Thomle, J., Day-Lewis, F., and Versteeg, R.J., 2022, Autonomous time-lapse electrical imaging for real-time management of subsurface systems, *The Leading Edge*, 41(8): 520 <https://doi.org/10.1190/tle41080520.1>
- Mangel, A.R., Dawson, C.B., Rey, D.M., and Briggs, M.A., 2022, Drone applications in hydrogeophysics: Recent examples and a vision for the future, *The Leading Edge* <https://doi.org/10.1190/tle41080540.1>.
- Nabighian, M.N. (ed.), 1991, ELECTROMAGNETIC METHODS IN APPLIED GEOPHYSICS: VOLUME 2, APPLICATION, PARTS A AND B, Society of Exploration Geophysicists, 991p.
- Scholl, V.M., Burgess, M.A., Bauer, M.A., Brady, L.R., and Thurau, R.G., 2024, Uncrewed Aircraft Systems (UAS) natural color, multispectral, lidar, and hyperspectral remote sensing data products collected at dryland sites 40 km south of Moab, Utah in May 2023: U.S Geological Survey data release, <https://doi.org/10.5066/P9MMCJET>.
- Terry, N., Day-Lewis, F.D., Lane, J.W., Johnson, C.D., and Werkema, D.L., 2023, Field evaluation of semi-automated moisture estimation from geophysics using machine learning, *Vadose Zone Journal*. <https://doi.org/10.1002/vzj2.20246>.
- Ward, S.H., Hohmann, G.W., 1987, Electromagnetic theory for geophysical applications. *Electromagnetic Methods in Applied Geophysics*. Society of Exploration Geophysicists, Tulsa, Oklahoma, pp. 131–311.
- Zhdanov, M. S., 2009, *Geophysical electromagnetic theory and methods*: Elsevier.

Pacific Northwest National Laboratory

902 Battelle Boulevard
P.O. Box 999
Richland, WA 99354

1-888-375-PNNL (7665)

www.pnnl.gov